Coupling Poisson-Nernst-Planck and Density Functional Theory to Calculate Ion Flux

Dirk Gillespie

Department of Physiology and Biophysics

University of Miami School of Medicine

P. O. Box 016430, Miami, FL 33101-6430, USA

dirkg@chroma.med.miami.edu

Wolfgang Nonner

Department of Physiology and Biophysics

University of Miami School of Medicine

P. O. Box 016430, Miami, FL 33101-6430, USA

wnonner@chroma.med.miami.edu

Robert S. Eisenberg

Department of Molecular Biophysics and Physiology

Rush Medical College

1750 W. Harrison St. #1291, Chicago, IL 60612, USA

beisenbe@rush.edu

June 1, 2002

Abstract

Ion transport between two baths of fixed ionic concentrations and applied electrostatic potential is analyzed using a one-dimensional drift-diffusion (Poisson-Nernst-Planck, PNP) transport system designed to model biological ion channels. The ions are described as charged, hard spheres with excess chemical potentials computed from equilibrium density functional theory. The method of Rosenfeld (J. Chem. Phys. **98**, 8126) is generalized to calculate the electrostatic excess chemical potential in channels. A numerical algorithm for solving the set of integral-differential PNP/DFT equations is described and used to calculate flux through a calcium-selective ion channel.

1 Introduction

The movement of ions through open ion channels is one of the many interesting physical chemistry problems presented by living cells. In this paper we describe a system to model such transport, using it as an example of a theory that may be applied to other problems of ion flux.

Cells and cell organelles are enveloped by lipid membranes that are nearly impermeable to physiological ions (mostly Na^+, K^+, Ca^{2+}, and Cl^-). One mechanism for ions to move across these membranes is through open ion channels, proteins embedded in the membrane that form ion-selective pores. This type of charge movement is used to conduct electrical signals down nerves and initiate muscle contraction, to list just two of the many physiological functions of ion channels [1].

Ion channels are proteins with functional groups that often are the side chains (residues) of charged amino acids. Enough data on these functional groups and even crystallographic channel structures are now available to apply specific theories of permeation and selectivity. With such information and theories it is possible to reverse engineer the devices that biologists observe, not only with the goal of understanding their natural function, but also of

controlling their function beyond biology.

In this paper we describe an engineering approach to selective ion conduction through ion channels. Specifically, we develop a one-dimensional model of the movement of ions between two baths of fixed ionic concentrations and applied electrostatic potentials. The baths are connected by a single open ion channel whose functional groups are represented as ions confined to the channel. In this model (unlike some we have studied [2], [3], [4]) ions are charged, hard spheres immersed in a hard-sphere solvent and uniform, continuum dielectric. Particle transport is described as friction-limited drift-diffusion with all excess chemical potentials described by the Density Functional Theory (DFT) of Rosenfeld and colleagues [5], [6], [7], [8], [9]. As an example, we present flux calculations for a simple model of a biological calcium channel. Although our specific goal is to model ion channels, the system is generally applicable to one-dimensional modeling of ion transport.

2 Geometry

The geometry of two baths connected by a single ion channel embedded in a membrane is shown in Fig. 1. This is the geometry of the most direct experiments [10], [11]. One inherent difficulty in modeling ion channels is the different length scales, with the nanometer-scale channel connected to the millimeter-scale baths where boundary conditions essential for the transport are maintained. Because the flux is controlled in the channel, the resolution must be high there. However, the boundary conditions of the problem must be applied far away from the channel to model the problem correctly. This problem is three dimensional, but a reasonable one-dimensional approximation can be developed that still includes the effects of the finite volume of ions and functional groups of the channel protein. In this section we derive an approximation that is fine grained in the flux-limiting region (the channel) and coarse grained in the baths. This approximation allows the problem to be solved on a desktop computer.

Starting in the baths, consider spherical shells that terminate at the lipid and are perpendicular to the lipid as well as the x-axis (Fig. 1). The flux of particles is perpendicular to these surfaces and therefore flux densities scale inversely with the area $A(x)$ of these shells. (The shells are indexed by their intersection with the x-axis.) This spherical geometry is exact for each bath alone: ions traveling to and from the channel must converge to a hemisphere given by the capture radius of the channel. As we move from the baths into the channel, we continue to assume that particles travel perpendicular to these spherical shells. Below we will argue that this is an appropriate approximation inside the channel where the spherical shells become flat, cross-sectional disks. In the transition regions this approximation is also valid. For example, in the calculation of the electric field in these transition regions, use of the spherical shells is equivalent to approximating a flat-bottomed cone by a spherical cone [12].

In the channel itself, it is important to consider the nature of the boundary between the pore (permeation pathway) and the channel protein that surrounds it. If the protein is described as a solid by a smooth, rigid wall at the protein/pore interface, then large radial packing effects are found inside the pore [13] and no mechanical effects extend into the protein. However, real proteins are not smooth or rigid, and therefore we take a different view of the protein/pore interface: the atoms of the channel protein are more like a liquid, forming a statistical boundary with the liquid in the pore. Such a boundary fluctuates around an average and therefore is not described by a geometric surface at a specific location, but rather by an *average* cross-sectional area or pore volume that may be constant or vary with local conditions depending on the compressibility of the protein [14]. In general, packing in the pore affects the interior of the protein by changing the local mechanical forces (pressure) inside the channel protein. Here we consider the case that the protein maintains a constant *average* cross-section for the pore fluid.

With this model of the protein/pore interface, both the input variables (the dielectric

coefficient and diffusion coefficients) and the output variables (the densities and electrostatic potential) become approximately constant in the plane perpendicular to the axis of the channel for the following reasons:

1. From the hard-sphere perspective, the protein spreads the radial influence of the ions in the pore beyond the cross-section actually filled by the permeating particles in the pore. Any radial space demands made by the particles in the pore will affect (radially) not only the contents of the pore, but also the atoms of the protein, which compete for space with the particles in the pore; atoms inside the protein feel the mechanical effect of the packing of ions in the pore because mechanical forces inside the pore spread across the interface into the protein. Seen as only a hard-sphere liquid, the combination of the pore and protein is approximately one continuous liquid.

2. In our geometric approximation, each cross-sectional disk is an equipotential surface and therefore there is no electric flux out of the pore; this is formally equivalent to the situation that the exterior of the pore has a dielectric coefficient of zero. The electric polarizability of the pore contents and the protein are not known, in particular on the time scale of ion conduction; in our description it is parameterized. However, because the lipid has a dielectric coefficient of approximately 2, as we move from the pore through the protein to the lipid, the zero dielectric coefficient approximation becomes better and better.

3. In the calcium channel described in Sec. 7 and other channels we will consider in future work, there are such large densities of structural and permeating ions inside the pore that the screening length becomes less than half the average radius of the pore. Brownian dynamics studies have shown that under this condition the induced charge at the protein/pore interface does not introduce a significant electrostatic energy penalty for ion entry into the pore [15], supporting the geometric approximation used here.

Our representation of the protein/pore interface is not just a means to obtain a one-dimensional approximation. We suggest that in future two- or three-dimensional calculations the protein should be modeled to include the two basic features discussed above: the hard-sphere interactions extend from the pore into the interior of the protein whereas the electrostatic interactions are essentially confined to the pore. The definition of the pore boundary follows the electrostatics.

3 Modeling ion flux

We describe steady-state flux by the constitutive law

$$-J_i = \frac{1}{kT} D_i(x) A(x) \rho_i(x) \frac{d\mu_i}{dx} \tag{1}$$

and the continuity equation

$$\frac{dJ_i}{dx} = 0; \tag{2}$$

that is, for particle species i, the (constant) flux J_i is proportional to the particle density $\rho_i(x)$ and the gradient of the electrochemical potential $\mu_i(x)$. $A(x)$ is the area of the spherical shells described in the previous section. This model was recently derived from a Poisson-Langevin system [16].

The electrochemical potential consists of the ideal component $\mu_i^{\mathrm{id}}(x)$, the excess component $\mu_i^{\mathrm{ex}}(x)$ from particle interactions, and the concentration-independent component $\mu_i^0(x)$:

$$\mu_i(x) = \mu_i^0(x) + \mu_i^{\mathrm{id}}(x) + \mu_i^{\mathrm{ex}}(x) \tag{3}$$

with

$$\mu_i^{\mathrm{id}}(x) = z_i e \phi(x) + kT \ln\left(\frac{\rho_i(x)}{\rho_{\mathrm{scale}}}\right) \tag{4}$$

where $\phi(x)$ is the local electrostatic potential, z_i is the valence of species i, and ρ_{scale} is some characteristic number density. $\mu_i^0(x)$ is, for example, a hard-wall potential. With these

definitions, Eq. (1) can be rewritten as a Poisson-drift-diffusion (Poisson-Nernst-Planck, PNP) system:

$$-J_i = D_i(x) A(x) \left[\frac{d\rho_i}{dx} + \frac{1}{kT} \rho_i(x) \left(z_i e \frac{d\phi}{dx} + \frac{d\mu_i^0}{dx} + \frac{d\mu_i^{\text{ex}}}{dx} \right) \right] \tag{5}$$

$$\frac{dJ_i}{dx} = 0 \tag{6}$$

$$-\frac{1}{A(x)} \frac{d}{dx} \left(\epsilon(x) A(x) \frac{d\phi}{dx} \right) = e \sum_i z_i \rho_i(x) \tag{7}$$

where $\epsilon(x)$ is the local dielectric coefficient. In this paper we consider the special case

$$\epsilon(x) = \text{constant} \tag{8}$$

so the Poisson equation we use is

$$-\frac{\epsilon}{A(x)} \frac{d}{dx} \left(A(x) \frac{d\phi}{dx} \right) = e \sum_i z_i \rho_i(x). \tag{9}$$

Position-dependent dielectric coefficients will be considered in future work.

4 Density functional theory

To calculate the excess chemical potentials μ_i^{ex} we use the density functional theory of Rosenfeld [6], [7]. We start by separating the grand potential into ideal (id), hard-sphere (HS), and electrostatic components (ES):

$$\Omega(\{\rho_k(\mathbf{x})\}) = \Omega_{\text{id}}(\{\rho_k(\mathbf{x})\}) + \Omega_{\text{HS}}(\{\rho_k(\mathbf{x})\}) + \Omega_{\text{ES}}(\{\rho_k(\mathbf{x})\}) \tag{10}$$

with

$$\Omega_{\text{id}}(\{\rho_k(\mathbf{x})\}) = kT \sum_i \int \rho_i(\mathbf{x}) \left[\ln\left(\frac{\rho_i(\mathbf{x})}{\rho_{\text{scale}}} \right) - 1 + \frac{z_i e}{kT} \phi(\mathbf{x}) + \frac{1}{kT} \left[\mu_i^0(\mathbf{x}) - \mu_i(\mathbf{x}) \right] \right] d\mathbf{x}. \tag{11}$$

The excess chemical potential μ_i^{ex} [Eq. (3)] is then the sum of the HS and ES components

$$\mu_i^{\text{ex}} = \mu_i^{\text{HS}} + \mu_i^{\text{ES}} \tag{12}$$

where

$$\mu_i^{\mathrm{HS}}(\mathbf{x}) = \frac{\delta\Omega_{\mathrm{HS}}(\{\rho_k(\mathbf{x}')\})}{\delta\rho_i(\mathbf{x})} \tag{13}$$

and

$$\mu_i^{\mathrm{ES}}(\mathbf{x}) = \frac{\delta\Omega_{\mathrm{ES}}(\{\rho_k(\mathbf{x}')\})}{\delta\rho_i(\mathbf{x})}. \tag{14}$$

The DFT describes equilibrium systems and thus our use of it in a steady-state transport system requires the approximation of local equilibrium. This approximation was validated by Frink, Thompson, and Salinger [17] who compared such a DFT-based description of diffusion in a hard-sphere fluid to grand canonical molecular dynamics simulations.

4.1 Hard-sphere component

For the hard-sphere component, we use the "antisymmetrized" excess free energy density [8, Eq. (27)] because it is the best currently available for particles in confined geometries:

$$\Phi_{\mathrm{HS}}(\{n_\alpha(\mathbf{x})\}) = -n_0\ln(1-n_3) + \frac{n_1n_2 - n_{V1}n_{V2}}{1-n_3} + \frac{n_2^3}{24\pi(1-n_3)^2}\left(1 - \frac{n_{V2}n_{V2}}{n_2^2}\right)^3 \tag{15}$$

with

$$\Omega_{\mathrm{HS}}(\{c_k(\mathbf{x})\}) = \int \Phi_{\mathrm{HS}}(\{n_\alpha(\mathbf{x}')\})\,d\mathbf{x}' \tag{16}$$

where

$$n_\alpha(\mathbf{x}) = \sum_i \int \rho_i(\mathbf{x}')\,\omega_i^{(\alpha)}(\mathbf{x}'-\mathbf{x})\,d\mathbf{x}' \qquad (\alpha = 0,1,2,3,V1,V2) \tag{17}$$

$$\omega_i^{(2)}(\mathbf{r}) = \delta(|\mathbf{r}| - R_i) \tag{18}$$

$$\omega_i^{(3)}(\mathbf{r}) = \theta(|\mathbf{r}| - R_i) \tag{19}$$

$$\omega_i^{(V2)}(\mathbf{r}) = \frac{\mathbf{r}}{|\mathbf{r}|}\delta(|\mathbf{r}| - R_i) \tag{20}$$

$$4\pi R_i^2\omega_i^{(0)}(\mathbf{r}) = 4\pi R_i\omega_i^{(1)}(\mathbf{r}) = \omega_i^{(2)}(\mathbf{r}) \tag{21}$$

$$4\pi R_i\omega_i^{(V1)}(\mathbf{r}) = \omega_i^{(V2)}(\mathbf{r}) \tag{22}$$

and R_i is the radius of species i. δ is the Dirac delta function and θ is the unit step function, $\theta(x>0)=0$ and $\theta(x\leq 0)=1$. Then the hard-sphere component μ_i^{HS} of μ_i^{ex} is given by [6], [7]

$$\mu_i^{\mathrm{HS}}(\mathbf{x}) = kT\sum_\alpha \int \frac{\partial \Phi_{\mathrm{HS}}}{\partial n_\alpha}(\mathbf{x}')\,\omega_i^{(\alpha)}(\mathbf{x}-\mathbf{x}')\,d\mathbf{x}'. \tag{23}$$

The integrals in Eqs. (17) and (23) simplify in the slab geometry. By analytically integrating over two components of the three-dimensional vector $\mathbf{x}$ and assuming that the functions $\rho_i(\mathbf{x})$ and $\partial\Phi_{\mathrm{HS}}/\partial n_\alpha(\mathbf{x})$ are constant over these two components, these integrals become [7]

$$n_\alpha(x) = \sum_i \int_{x-R_i}^{x+R_i} \rho_i(x')\,W_i^{(\alpha)}(x'-x)\,dx' \tag{24}$$

$$\mu_i^{\mathrm{HS}}(x) = kT\sum_\alpha \int_{x-R_i}^{x+R_i} \frac{\partial \Phi_{\mathrm{HS}}}{\partial n_\alpha}(x')\,W_i^{(\alpha)}(x-x')\,dx' \tag{25}$$

where

$$W_i^{(2)}(r) = 2\pi R_i \tag{26}$$

$$W_i^{(3)}(r) = \pi\left(R_i^2 - r^2\right) \tag{27}$$

$$W_i^{(V2)}(r) = 2\pi r\,(1,0,0) \tag{28}$$

$$4\pi R_i^2 W_i^{(0)}(r) = 4\pi R_i W_i^{(1)}(r) = W_i^{(2)}(r) \tag{29}$$

$$4\pi R_i W_i^{(V1)}(r) = W_i^{(V2)}(r). \tag{30}$$

4.2 Electrostatic component

For the electrostatic component μ_i^{ES} of μ_i^{ex} we use a generalization of Rosenfeld's method [7] of expanding Ω_{ES} in a functional Taylor series in powers of

$$\Delta\rho_i(\mathbf{x}) = \rho_i(\mathbf{x}) - \rho_i^{\mathrm{ref}}(\mathbf{x}) \tag{31}$$

where $\rho_i^{\mathrm{ref}}(\mathbf{x})$ is a given, nonuniform reference density profile. Then, up to second order,

$$\begin{aligned}\Omega_{\mathrm{ES}}\left(\{\rho_k(\mathbf{x})\}\right) \approx & \Omega_{\mathrm{ES}}\left(\left\{\rho_k^{\mathrm{ref}}(\mathbf{x})\right\}\right)+kT\sum_i\int\mu_i^{\mathrm{ES}}\left(\left\{\rho_k^{\mathrm{ref}}(\mathbf{x})\right\}\right)\Delta\rho_i(\mathbf{x})\,d\mathbf{x} \\ & -\frac{kT}{2}\sum_{i,j}\int\int c_{ij}^{(2),\mathrm{ES}}(\mathbf{x},\mathbf{x}')\,\Delta\rho_i(\mathbf{x})\,\Delta\rho_j(\mathbf{x}')\,d\mathbf{x}d\mathbf{x}' \\ & -\sum_i z_i e\int\rho_i(\mathbf{x})\,\phi(\mathbf{x})\,d\mathbf{x}\end{aligned} \tag{32}$$

where $c_{ij}^{(2),\mathrm{ES}}$ is the electrostatic component of the second-order direct correlation function of the reference fluid [7]. Eq. (14) gives [7], [9]

$$\mu_i^{\mathrm{ES}}(\mathbf{x})=\mu_i^{\mathrm{ES}}\left(\left\{\rho_k^{\mathrm{ref}}(\mathbf{x})\right\}\right)-kT\sum_j\int c_{ij}^{(2),\mathrm{ES}}(\mathbf{x},\mathbf{x}')\,\Delta\rho_j(\mathbf{x}')\,d\mathbf{x}'-z_i e\phi(\mathbf{x})\,. \tag{33}$$

4.2.1 Reference fluid component

In Rosenfeld's implementation [7] the reference fluid was the bulk (homogeneous) fluid that was in equilibrium with the inhomogeneous fluid. In the study of ion channels this will not suffice, however, as the regions of the system are very diverse. Channels are embedded in a membrane that separates two bulk fluids whose ionic concentrations are different, experimentally controlled, and can range from < 1 μM to 2 M. More importantly, inside the channel there is a very high density of charges from the amino acid residues of the channel protein. These attract equally high concentrations of counter charge with the total concentration of tens of molar. Thus, each section of the geometry has a different "intrinsic" reference fluid composition.

To define the reference densities $\rho_k^{\mathrm{ref}}(\mathbf{x})$ for all species (permeating and confined) assume that some densities $\rho_k^*(\mathbf{x})$ and an estimate of the screening length at every point $s^*(\mathbf{x})$ are given. (These will later be determined by a self-consistency iteration.) From these given densities we will construct a reference fluid that is charge-neutral and described by average, non-local densities.

To determine the $\rho_k^{\mathrm{ref}}(\mathbf{x})$, we start by defining

$$\bar{\rho}_k(\mathbf{x}) = A\rho_k^*(\mathbf{x}) \qquad (z_k \geq 0) \tag{34}$$

and

$$\bar{\rho}_k(\mathbf{x}) = AB\rho_k^*(\mathbf{x}) \qquad (z_k < 0) \tag{35}$$

with the constants A and B determined by requiring the $\{\bar{\rho}_k(\mathbf{x})\}$ to be charge-neutral and to have the same ionic strength at each location $\mathbf{x}$ as the $\{\rho_k^*(\mathbf{x})\}$; that is, we require that

$$0 = \sum_k z_k \bar{\rho}_k(\mathbf{x}) \tag{36}$$

and

$$\sum_k z_k^2 \bar{\rho}_k(\mathbf{x}) = \sum_k z_k^2 \rho_k^*(\mathbf{x}). \tag{37}$$

These conditions give

$$A = \frac{\sum_k z_k^2 \rho_k^*(\mathbf{x})}{\sum_{z_k \geq 0} z_k^2 \rho_k^*(\mathbf{x}) + B\sum_{z_k<0} z_k^2 \rho_k^*(\mathbf{x})} \tag{38}$$

and

$$B = \frac{\sum_{z_k \geq 0} z_k \rho_k^*(\mathbf{x})}{\sum_{z_k<0} |z_k| \rho_k^*(\mathbf{x})}. \tag{39}$$

The $\rho_k^{\mathrm{ref}}(\mathbf{x})$ are then defined as spatially averaged $\bar{\rho}_k(\mathbf{x})$:

$$\rho_k^{\mathrm{ref}}(\mathbf{x}) = \int \bar{\rho}_k(\mathbf{x}')\, w(\mathbf{x}', \mathbf{x})\, d\mathbf{x}' \tag{40}$$

where the weight function w is a normalized form of the volume weight $\omega_i^{(3)}$ (Eq. (19)):

$$w(\mathbf{x}', \mathbf{x}) = \frac{\theta(|\mathbf{x}' - \mathbf{x}| - R_{\mathrm{filter}}(\mathbf{x}))}{\frac{4\pi}{3} R_{\mathrm{filter}}^3(\mathbf{x})}. \tag{41}$$

The radius of the sphere over which we average is an approximation of the electrostatic length scale, namely the capacitance radius (that is, the ion radius plus the screening length):

$$R_{\mathrm{filter}}(\mathbf{x}) = \frac{\sum_k \bar{\rho}_k(\mathbf{x}) R_k}{\sum_k \bar{\rho}_k(\mathbf{x})} + s^*(\mathbf{x}). \tag{42}$$

The averaging produces a kind of non-local reference density, removing discontinuities that may have been in the $\{\bar{\rho}_k(\mathbf{x})\}$. Futhermore, because we use the same filter and filter length for each species k, the resulting $\left\{\rho_k^{\mathrm{ref}}(\mathbf{x})\right\}$ are charge-neutral at every point since the $\{\bar{\rho}_k(\mathbf{x})\}$ are.

To calculate the ES excess chemical potential of the reference fluid, we apply the MSA for bulk fluids at every point [18]. This not only results in values for $\mu_i^{\mathrm{ES}}\left(\left\{\rho_k^{\mathrm{ref}}(\mathbf{x})\right\}\right)$, but also for the screening length, which we now redefine as

$$s(\mathbf{x}) = \frac{1}{2\Gamma(\mathbf{x})} \tag{43}$$

where $\Gamma(\mathbf{x})$ is the MSA parameter Γ that has been calculated at every point $\mathbf{x}$. This then defines the capacitance length of each ion species:

$$\lambda_k(\mathbf{x}) = R_k + s(\mathbf{x}). \tag{44}$$

In this procedure, the approximate screening length $s^*(\mathbf{x})$ is used to calculate the reference densities $\left\{\rho_k^{\mathrm{ref}}(\mathbf{x})\right\}$, and from these densities the corrected screening length $s(\mathbf{x})$ is calculated. At each point this screening length can be substantially different from the original $s^*(\mathbf{x})$ and therefore we iterated the screening length to self-consistency with the following method:

1. Starting with $\{\rho_k^*(\mathbf{x})\}$ and $s^*(\mathbf{x})$, calculate the starting (zeroeth) values $\left\{\rho_k^{\mathrm{ref}}(\mathbf{x})_0\right\}$ and $s(\mathbf{x})_0$ as described.

2. Using the original $\{\rho_k^*(\mathbf{x})\}$ but the m-th screening length $s(\mathbf{x})_m$, calculate $\left\{\rho_k^{\mathrm{ref}}(\mathbf{x})\right\}$ as described.

3. Define the $m+1$-th reference fluid densities $\left\{\rho_k^{\mathrm{ref}}(\mathbf{x})_{m+1}\right\}$ as

$$\rho_k^{\mathrm{ref}}(\mathbf{x})_{m+1} = \frac{\rho_k^{\mathrm{ref}}(\mathbf{x})_m + \alpha\rho_k^{\mathrm{ref}}(\mathbf{x})}{1+\alpha}. \tag{45}$$

   We found $\alpha = 1$ to work well.

4. If

$$\max_{\mathbf{x}} |s_m(\mathbf{x}) - s_{m-1}(\mathbf{x})| \leq 10^{-5} \text{ nm}, \tag{46}$$

then the iteration is stopped.

At the end of the iteration, we obtain the reference fluid densities $\left\{\rho_k^{\text{ref}}(\mathbf{x})\right\}$ and the screening length $s(\mathbf{x})$ that is consistent with those densities as well as $\mu_i^{\text{ES}}\left(\left\{\rho_k^{\text{ref}}(\mathbf{x})\right\}\right)$. These values are then used in the PNP/DFT calculations. We have not, however, specified how to choose the input densities $\{\rho_k^*(\mathbf{x})\}$ from which the reference fluid densities are calculated. This will be done in Sec. 4.3 where we describe an algorithm to iterate the solution of the entire PNP/DFT system to self-consistency by choosing the $\{\rho_k^*(\mathbf{x})\}$ to calculate better and better reference fluid densities $\left\{\rho_k^{\text{ref}}(\mathbf{x})\right\}$ by the method described in this section. For flux problems we found that to have the PNP/DFT iterate to self-consistency (Sec. 4.3), it was necessary to use screening lengths consistent with the reference fluid.

4.2.2 Non-reference fluid component

Calculating the second term of Eq. (33) requires the correlation function of the reference fluid $c_{ij}^{(2),\text{ES}}(\mathbf{x},\mathbf{x}')$. We start by approximating the direct correlation function with the MSA [19]:

$$c_{ij}^{(2),\text{ES}}(\mathbf{x},\mathbf{x}') = -\frac{1}{kT}\psi_{ij}(\mathbf{x},\mathbf{x}') \tag{47}$$

if

$$|\mathbf{x}-\mathbf{x}'| > R_{ij} = R_i + R_j \tag{48}$$

where $\psi_{ij}(\mathbf{x},\mathbf{x}')$ is the interaction potential of two point particles with charge $z_i e$ and $z_j e$ located at $\mathbf{x}$ and $\mathbf{x}'$, respectively. In the case of uniform dielectric coefficient,

$$\psi_{ij}(\mathbf{x},\mathbf{x}') = \frac{z_i z_j e^2}{4\pi\epsilon\epsilon_0}\frac{1}{|\mathbf{x}-\mathbf{x}'|}. \tag{49}$$

Since [9]

$$kT\sum_j \int \psi_{ij}(\mathbf{x},\mathbf{x}')\,\rho_j(\mathbf{x}')\,d\mathbf{x}' = z_i e\phi(\mathbf{x}), \tag{50}$$

we have

$$\mu_i^{\mathrm{ES}}(\mathbf{x}) = \mu_i^{\mathrm{ES}}\left(\left\{\rho_k^{\mathrm{ref}}(\mathbf{x})\right\}\right) - kT\sum_j \int_{|\mathbf{x}-\mathbf{x}'|\le R_{ij}} \left(c_{ij}^{(2),\mathrm{ES}}(\mathbf{x},\mathbf{x}') + \psi_{ij}(\mathbf{x},\mathbf{x}')\right)\Delta\rho_j(\mathbf{x}')\,d\mathbf{x}' \tag{51}$$

where the core-overlap electrostatic correlations remain to be determined. Our choice for this ES correlation function is an approximation of the analytic bulk MSA ES correlation function [20] given by Blum and Rosenfeld [21, Eq. (56)] that the ES correlation function $c_{ij}^{(2),\mathrm{ES}}$ is the negative of the interaction potential of two spherical shells Θ_i and Θ_j with each Θ_k having uniformly smeared charge equal and opposite that of the ion species k and radius λ_k, the capacitance radius of ion species k defined by Eq. (44). With this ansatz,

$$\begin{aligned} &kT\left(c_{ij}^{(2),\mathrm{ES}}(\mathbf{x},\mathbf{x}') + \psi_{ij}(\mathbf{x},\mathbf{x}')\right) \\ &= -\frac{z_i z_j e^2}{8\pi\epsilon\epsilon_0}\frac{1}{|\mathbf{x}-\mathbf{x}'|}\left(|\mathbf{x}-\mathbf{x}'|\frac{\lambda_i+\lambda_j}{\lambda_i\lambda_j} - \frac{|\mathbf{x}-\mathbf{x}'|^2}{2\lambda_i\lambda_j} - \frac{(\lambda_i-\lambda_j)^2}{2\lambda_i\lambda_j}\right) \end{aligned} \tag{52}$$

In the slab geometry, Eq. (51) then becomes

$$\begin{aligned} \mu_i^{\mathrm{ES}}(x) =& \mu_i^{\mathrm{ES}}\left(\left\{\rho_k^{\mathrm{ref}}(x)\right\}\right) - \sum_j \frac{z_i z_j e^2}{8\epsilon\epsilon_0}\frac{1}{\lambda_i\lambda_j} \\ &\times \int_{x-R_{ij}}^{x+R_{ij}} c_i(x')\left(\frac{1}{3}R_{ij}^3 + \lambda_{ij}^2 R_{ij} - \lambda_{ij}R_{ij}^2 + \lambda_{ij}(x'-x)^2\right. \\ &\left. -\frac{1}{3}|x'-x|^3 - \lambda_{ij}^2|x'-x|\right)dx' \end{aligned} \tag{53}$$

where

$$\lambda_{ij} = \lambda_i + \lambda_j. \tag{54}$$

4.3 Iterating to self-consistency

The choice of reference fluid is particularly important because it must be close enough to the final solution of the system that $\Delta\rho_k(\mathbf{x})$ is small so that the expansion of the ES grand potential (32) is valid. We achieve this by iteration on the choice of reference fluid. A

guess of the solution serves as the initial set of $\{\rho_k^*(\mathbf{x})\}$ from which the reference densities are calculated as described in Sec. 4.2.1. The initial screening length $s^*(\mathbf{x})$ is set to zero everywhere. The system of equations is solved using this reference fluid and the screening and capacitance lengths defined in Eqs. (43) and (44), respectively. The densities from this solution then become the $\{\rho_k^*(\mathbf{x})\}$ for the next iteration cycle. After two iterations we observe no significant differences in the solutions. For the results shown in this paper we used three iterations.

4.4 Tests of the solution method

To ensure that our DFT method is valid, we compare our results for an equilibrium problem to Monte Carlo (MC) simulations [22], [23]. In the simulations, two compartments of different ionic compositions are equilibrated in the primitive model. In the left bath is a 24 M solution of half-charged oxygen ions that is confined to that compartment by a hard-wall potential. In the right bath is a 0.1 M ionic solution. We conducted three separate tests with $CaCl_2$, NaCl, or KCl in the right compartment.

For these test simulations, the equations are solved as described below (Sec. 6) except that because the test is an equilibrium problem we do not solve the Nernst-Planck equations (5), but rather

$$\mu_k(x) = \mu_k \tag{55}$$

where the total electrochemical potential μ_k was given for each ion species k. The results of the simulations (shown in Figs. 2 and 3) are quite good. In order to achieve this close match, it was essential that the ES correlation function (Eq. (52)) and the spatial averaging of the reference densities (Eq. (40)) accounted for the substantial variations of the screening length between the two compartments (in the case of NaCl, 0.167 nm in the left compartment and 1.08 nm in the right compartment); otherwise the density variations in the boundary layer were poorly reproduced.

The particular ions and concentrations are chosen to approximate the calcium channel for which we later calculate current/voltage curves (Sec. 7). We vary the cation species so that the accuracy we obtain bears directly on our ability to model ion selectivity.

Although we do not show them here, in separate tests, we also compared our equilibrium DFT calculations using a uniform reference fluid to previously published MC simulations [23], [24]. The comparisons were excellent.

5 Modeling the selectivity filter

Ion channels are proteins that can control permeation by placing some of their amino acid residues into the pore where their groups interact as tethered but otherwise mobile particles with the permeating particles (both ions and solvent). It is these residues (many of which are charged) that confer the selectivity properties of the channel. For example, in the L-type calcium channel, there are four highly-conserved glutamate (E) residues (the "EEEE" locus) in the "selectivity filter" that produce the large physiological selectivity of calcium over sodium and potassium [25], [26], [27]. Voltage-gated sodium channels, on the other hand, have other conserved amino acids, namely aspartate (D), glutamate, lysine (K), and alanine (A) (the "DEKA" locus). Furthermore, if these are mutated to DEEE, then the channel becomes calcium selective under physiological conditions [28], [29].

In equilibrium studies, these essential "structural charges" have been modeled as ions that are allowed to move freely inside the selectivity filter, but are confined there; they cannot partition into the baths on each side of the channel [14], [29], [30], [31], [32]. We use the same approach here. Because these ions never reach the electrodes in the bath, they do not contribute to the measured current; each confined species j is in equilibrium:

$$\nabla \mu_j = 0. \tag{56}$$

It is not a priori known what the value of the chemical potential μ_j is. What is known,

however, is that the number of particles of each confined species j (N_j) is fixed. Therefore, in conjunction with Eq. (56), for each confined species we solve the equation

$$\int \rho_j(\mathbf{x})\, d\mathbf{x} = N_j \tag{57}$$

where the integral is over the region of confinement. In our geometry, this becomes

$$\int_{x_L}^{x_R} A(x)\, \rho_j(x)\, dx = N_j \tag{58}$$

the range of confinement is from x_L to x_R (the range of the selectivity filter).

Structural particles that are ions contribute to the electric field and therefore are also included in the Poisson equation (9) that calculates the electrostatic potential experienced by the permeating ions. However, because there is a small number of confined particles, if the mean electrostatic potential from Eq. (9) were used to calculate the electrochemical potential of the confined particles, then each confined particle would interact with a field that includes a contribution from the particle itself. This is a problem inherent to the mean-field approach, but one that is significant only when there are a finite number of ions of one species. The problem is best seen if one species consists of a single particle; if that ion is included in the mean electric field that acts on that single ion, then the calculation is incorrect because the ion acts directly on itself. In calculations without a correction, the density of a single charge repels itself and assumes an obviously artifactual spatial distribution.

We alleviate the error introduced by such self-interaction by calculating the electrochemical potential of the confined particles with a different electrostatic potential for each confined species that applies only to that confined particle species. Specifically, in the calculation of μ_j, the electrostatic potential ϕ_j for confined species j is calculated from the modified Poisson equation

$$-\frac{\epsilon}{A(x)}\frac{d}{dx}\left(A(x)\frac{d\phi_j}{dx}(x)\right) = e\sum_{k\neq j} z_k\rho_k(x) + ez_j\frac{N_j-1}{N_j}\rho_j(x) \tag{59}$$

where the density of confined species j is reduced by $\rho_j(x)/N_j$ to approximately eliminate the self-interaction.

6 Numerical implementation

The inputs to the problem are the left and right far-bath concentrations of the permeating particles (ions and solvent), the applied electrostatic potential, and the number of structural (confined) ions, as well as the radii and diffusion coeffients of all particles and the dielectric coefficient. The outputs are the densities of all particles (permeating and structural) and the electrostatic potential, both as functions of location. These are found by simultaneously solving Eqs. (5), (6), (9), (25), (53), (56), (57), and (59). After these have been solved, fluxes are computed from an integrated Nernst-Planck equation (5):

$$J_i = \frac{\exp\left(\frac{\mu_i(L)}{kT}\right) - \exp\left(\frac{\mu_i(R)}{kT}\right)}{\int \exp\left(\frac{\mu_i(x)}{kT}\right) \left[\rho_i(x) D_i(x) A(x)\right]^{-1} dx} \tag{60}$$

where the integral is over the entire system and $\mu_i(L/R)$ are the given left (L) and right (R) bath chemical potentials.

6.1 Discretization

The grid we choose is nonuniform because the baths are necessarily much longer than the channel to which the structural charges are confined and, because the baths are of fixed concentration far from the channel, do not require the high density of grid points that the channel does where the functions are changing rapidly. In the channel we choose a grid with uniform spacing of 0.02 nm. (Numerical tests showed no significant differences when smaller spacings were used.) The spacing of the nonuniform grid outside the channel is chosen to be proportional to $A(x)$, the area available for flux (Fig. 1) [4].

The differential equations (5), (6), (9), and (59) are rewritten as follows before they are discretized:

$$0 = \frac{d}{dx}\left[F_i(x)\frac{d}{dx}\left(u_i + \frac{z_i e}{kT}\phi(x) + \frac{1}{kT}\mu_i^0(x) + \frac{1}{kT}\mu_i^{\text{ex}}(x)\right)\right] \tag{61}$$

$$u_i(x) = \ln\left[\rho_i(x)\right] \tag{62}$$

$$F_i(x) = \frac{D_i(x) A(x)}{\min_x \{D_i(x) A(x)\}} \exp[u_i(x)] \tag{63}$$

$$-\frac{\epsilon\epsilon_0 kT}{e^2 d^2 \rho_{\text{scale}}} \frac{1}{A(x)} \frac{d}{dx}\left(A(x) \frac{d\phi}{dx}\right) = \sum_i z_i \exp[u_i(x)] \tag{64}$$

where all densities have been scaled by Avogadro's number (N_A) per liter (1 Molar) with

$$\rho_{\text{scale}} = 1000 N_A \tag{65}$$

and all lengths have been scaled by the system length d. (Eq. (59) may be rewritten in a similar form as Eq. (64)).

Both the recast Nernst-Planck equation (61) and the recast Poisson equation (64) have the same form for the derivatives:

$$\frac{d}{dx}\left(f(x) \frac{dy}{dx}\right). \tag{66}$$

We discretize this derivative on the interior points of the grid $\{x_0 = 0, x_1, x_2, \ldots, x_{N-1}, x_N = 1\}$ by

$$\begin{aligned}
&\frac{d}{dx}\left(f(x) \frac{dy}{dx}\right) \\
\approx &\frac{2}{h_m + h_{m+1}} \left[f_{m+\frac{1}{2}} \frac{dy}{dx}\left(x_{m+\frac{1}{2}}\right) - f_{m-\frac{1}{2}} \frac{dy}{dx}\left(x_{m-\frac{1}{2}}\right)\right] &(67)\\
\approx &\frac{2}{h_m + h_{m+1}} \left[\frac{f_m + f_{m+1}}{2} \frac{y_{m+1} - y_m}{h_{m+1}} - \frac{f_{m-1} + f_m}{2} \frac{y_m - y_{m-1}}{h_m}\right] &(68)\\
= &(f_m + f_{m+1})(y_{m+1} - y_m) \beta_{1,m} - (f_{m-1} + f_m)(y_m - y_{m-1}) \beta_{-1,m} &(69)
\end{aligned}$$

where

$$f_m = f(x_m) \tag{70}$$

$$y_m = y(x_m) \tag{71}$$

$$\beta_{m,-1} = \frac{1}{h_m (h_{m+1} + h_m)} \qquad \beta_{m,1} = \frac{1}{h_{m+1} (h_{m+1} + h_m)} \tag{72}$$

$$h_m = x_m - x_{m-1}. \tag{73}$$

This is finally rewritten as

$$\begin{aligned}
&\frac{d}{dx}\left(f(x)\frac{dy}{dx}\right) \\
\approx&\beta_{-1,m}\left(f_{m-1}+f_m\right)y_{m-1}-\left[\beta_{-1,m}\left(f_{m-1}+f_m\right)+\beta_{1,m}\left(f_m+f_{m+1}\right)\right]y_m \\
&+\beta_{1,m}\left(f_m+f_{m+1}\right)y_{m+1}.
\end{aligned} \tag{74}$$

All functions are specified on the boundary nodes x_0 and x_N, either because the function has been specified for all grid points (the diffusion coefficients, for example) or because of boundary conditions for the problem (the densities, for example). Thus these derivatives are defined on the interior grid points, $x_1, \ldots, x_{N-1}$.

The integrals in Eqs. (24), (25), and (53) have a similar structure and thus the integration scheme we choose is the same for all three. These integrals are over the range $x-r$ to $x+r$ with different r's for each integral. x is always a grid point, but r is a radius and because of the nonuniform grid and different ion sizes, it not generally true that $x-r$ or $x+r$ are grid points. Thus it is necessary to be able to evaluate these integrals at points between two grid nodes. We do this by dividing the integral into a sum of integrals, with each new integral ranging over two consecutive grid points or the last grid point to the endpoint of the original integral. Since in Eqs. (24), (25), and (53) one of the functions can be written as a polynomial in the integration variable x', each new integral in the sum can be evaluated analytically by assuming that the other function in the integral ($\rho_i(x')$ or $\partial\Phi_{\mathrm{HS}}/\partial n_\alpha(x')$) is a linear function in x' between consecutive grid nodes.

The remaining equations to be discretized are Eqs. (56) and (57) for the confined particles. Let x_{M_L} and x_{M_R} be the left and right grid nodes, respectively, on and between which the structural particles are confined. Then Eq. (56) is discretized as

$$0=\mu_j(x_m)-\mu_j(x_{m+1}) \tag{75}$$

for $M_L \le m \le M_R-1$. For the last grid node of confinement x_{M_R}, we apply Eq. (57). Because this integral is always evaluated only in the region where the grid spacing is uniform

and small, we discretize this with the trapezoidal rule.

6.2 Solving the discretized system

After the system of equations is discretized, the values of $u_i(x_m) = \ln[\rho_i(x_m)]$ for all permeant species i and $\phi(x_m)$ remain to be determined at all interior grid points ($m = 1, \ldots, N-2$), as well as $u_j(x_m) = \ln[\rho_i(x_m)]$ and $\phi_j(x_m)$ for all confined species j at all grid points to which they are confined ($m = M_L, \ldots, M_R$). We solve the system of discretized equations using Newton's method [33] because of its square-convergence properties, because it is possible to analytically evaluate the Jacobian (derivative) matrix of the discretized equations, and, most importantly, because iterative methods that did not update *all* variables at *every* iteration did not converge, or required a very large number of iterations. Using Newton's method with a poor initial guess, 30 iterations are typical with a total calculation time of one to two minutes on a desktop machine, depending on the number ion species. Many fewer iterations (4-10) are necessary when a better inital guess is available, for example when calculating a current/voltage curve. Then a good initial guess is a previous solution of the system with a different applied voltage.

Because of the specific functional dependence of the equations, it is possible to write the Jacobian matrix as a band matrix. Furthermore, without the discretized version of Eq. (57) the band becomes significantly more narrow. Because Eq. (57) is a solution condition for Eq. (56) and is only used once for each confined species, it is more efficient to solve the Jacobian matrix equation for each Newton iteration in two steps, first solving the narrow band matrix without Eq. (57) using an LU decomposition for band matrices [33] and finally solving the complete Newton matrix equation with the Sherman-Morrison-Woodbury method [33]. The Newton iteration was stopped when the absolute value of the largest difference between the same variable from two consecutive iterations was less than 10^{-8}.

7 Example: a calcium channel

To give an example of a flux system, we model a calcium-selective channel. In this channel, the structural particles are four fully-charged glutamate residues as those found in the L-type calcium channel [4], [14]. We model each glutamate residue by the carboxyl group at its end. Each of these carboxyls we describe as two unbonded, half-charged oxygen ions that are confined with a hard-wall potential to the cylindrical selectivity filter (channel) of radius 0.4 nm and length 1 nm. In the outer quarters of the filter, an extra linear repulsive potential ($\mu^0_{\mathrm{Ox}}(x)$) is applied to further confine the oxygens to the middle of the filter, with μ^0_{Ox} changing 1 kT per 0.1 nm.

Throughout the system we assume that the dielectric coefficient is uniform with $\epsilon = 78.4$, the value for pure water. Previous studies have estimated that inside the channel an dielectric coefficient of approximately 10 is needed to have the channel select calcium in the micromolar range as the real protein does [14]; the choice of a uniform dielectric coefficient will cause our simulated channel to be less selective than the real channel. Furthermore, these studies showed that including water as uncharged, hard spheres gives significantly different results than using the primitive model, and therefore in the current simulations we also include water in this way. The values of the other external parameters are listed in the legend of Fig. 4.

For this channel we simulate the classic selectivity experiment of the L-type calcium channel in which the left and right baths contain 100 mM NaCl and $CaCl_2$ is added to the right (extracellular) bath [34], [35], [36]. In Fig. 4 are shown the electrostatic potential and concentration profiles of H_2O, $O^{-1/2}$, Ca^{2+}, Na^+, and Cl^- for different $CaCl_2$ concentrations in the right bath. As $CaCl_2$ is added, Na^+ is displaced from the channel, with 1 mM of Ca^{2+} displacing most of the Na^+. The model channel is calcium selective over sodium.

The exchange of the cations is accompanied by small redistributions of the oxygen ions and substantial changes in the electrostatic potential. The potential in the pore is much less

negative with Ca^{2+} than with Na^+ as the dominant counterion. Since the mean electrostatic potential in the pore reflects both the applied potential (-50 mV in the case shown in Fig. 4) and the screening of the oxygens by the two counterions, Na^+ and Ca^{2+}, this indicates that screening by Ca^{2+} in the pore is stronger than screening by Na^+. The other permeating particles, Cl^- and water, play smaller roles in the selectivity; Cl^- is excluded by the channel in the presence of either cation while the water density in the channel is complementary to that of the oxygen ions (which occupy much of the volume).

Fig. 5 shows current/voltage relations for the four Ca^{2+} bath concentrations used in Fig. 4. The currents for the two smallest Ca^{2+} concentrations (10^{-7} and 10^{-5} M) are almost linear, whereas those found in larger calcium concentrations (10^{-3} and 10^{-1} M) are nonlinear. The nonlinearity is due to a varying occupancy of the filter by Ca^{2+}; more Ca^{2+} enters the pore when a negative potential is applied to the left (intracellular) bath and attracts Ca^{2+} from the right (extracellular) bath into the pore. Ca^{2+} in this example has been assigned a smaller diffusion coefficient than Na^+ in the pore; thus currents carried by Ca^{2+} are smaller than currents carried by Na^+. The pattern of currents shown in Fig. 5 corresponds qualitatively to that seen in biological calcium channels, but Na^+ is displaced at higher Ca^{2+} bath concentrations than in the biological channel. Our model as described gives substantial calcium selectivity, but other aspects (such as a low dielectric coefficient in the pore) are needed to fully model the natural channel.

8 Conclusion

We have developed a model to calculate ion flux through ion channels (although the model is more general) and an algorithm to solve it. The model is computationally inexpensive while at the same time representing essential features of both the ions (charge and excluded volume) and the channel protein (charged residues that interact with the permeating particles while not maintaining a fixed, hard structure around the pore). An application to a simple

model of a calcium-selective channel shows that the charge/space competition created by ions in a confined geometry results in significant selectivity of Ca^{2+} over Na^{+}.

Acknowledgments

This work was supported by grants from DARPA (R.S.E. and W.N.) and NIH (T32NS07044 to D.G.). We are most grateful to Dezső Boda who provided the Monte Carlo simulations we used to verify the DFT calculations in Figs. 2 and 3.

References

[1] B. Hille, *Ion Channels of Excitable Membranes,* 3rd ed. (Sinauer Associates, Inc., Sunderland, MA, 2001).

[2] D. P. Chen, J. Lear, and B. Eisenberg, Biophys. J. **72**, 97 (1997).

[3] D. P. Chen, L. Xu, A. Tripathy, G. Meissner, and B. Eisenberg, Biophys. J. **76**, 1346 (1999).

[4] W. Nonner and B. Eisenberg, Biophys. J. **75**, 1287 (1998).

[5] C. Caccamo, J.-P. Hansen, and G. Stell, *New Approaches to Problems in Liquid State Theory: Inhomogeneities and Phase Separation in Simple, Complex, and Quantum Fluids* (Kluwer Academic Publishers, Dordrecht, The Netherlands, 1999).

[6] Y. Rosenfeld, Phys. Rev. Lett. **63**, 980 (1989).

[7] Y. Rosenfeld, J. Chem. Phys. **98**, 8126 (1993).

[8] Y. Rosenfeld, M. Schmidt, H. Löwen, and P. Tarazona, Phys. Rev. E **55**, 4245 (1997).

[9] T. Biben, J.-P. Hansen, and Y. Rosenfeld, Phys. Rev. E **57**, R3727 (1998).

[10] B. Sakmann and E. Neher, eds., *Single-Channel Recording* (Plenum Press, New York, 1983).

[11] O. P. Hamill, A. Marty, E. Neher, B. Sakmann, and F. J. Sigworth, Pflügers Arch. **391**, 85 (1981).

[12] J. D. Romano and R. H. Price, Am. J. Phys. **64**, 1150 (1996).

[13] D. Goulding, S. Melchionna, and J.-P. Hansen, Phys. Chem. Chem. Phys. **3**, 1644 (2001).

[14] W. Nonner, D. Gillespie, D. Henderson, and B. Eisenberg, J. Phys. Chem. B **105**, 6427 (2001).

[15] B. Corry, S. Kuyucak, and S.-H. Chung, Biophys. J. **78**, 2364 (2000).

[16] Z. Schuss, B. Nadler, and B. Eisenberg, Phys. Rev. E **64**, 036116 (2001).

[17] L. J. D. Frink, A. Thompson, and A. G. Salinger, J. Chem. Phys. **112**, 7564 (2000).

[18] L. Blum, Mol. Phys. **30**, 1529 (1975).

[19] E. Waisman and J. L. Lebowitz, J. Chem. Phys. **56**, 3086 (1972).

[20] K. Hiroike, Mol. Phys. **33**, 1195 (1977).

[21] L. Blum and Y. Rosenfeld, J. Stat. Phys. **63**, 1177 (1991).

[22] D. Boda, K. Y. Chan, and D. Henderson, J. Chem. Phys. **109**, 7362 (1998).

[23] D. Boda, D. Henderson, R. Rowley, and S. Sokołowski, J. Chem. Phys. **111**, 9382 (1999).

[24] D. Boda, D. Henderson, A. Patrykiejew, and S. Sokołowski, J. Chem. Phys. **113**, 802 (2000).

[25] G. Mikala, A. Bahinski, A. Ytani, S. Tang, and A. Schwartz, FEBS Lett. **335**, 265 (1993).

[26] J. Yang, P. T. Ellinor, W. A. Sather, J. F. Zhang, and R. Tsien, Nature **366**, 158 (1993).

[27] P. T. Ellinor, J. Yang, W. A. Sather, J.-F. Zhang, and R. Tsien, Neuron **15**, 1121 (1995).

[28] S. H. Heinemann, H. Terlau, W. Stühmer, K. Imoto, and S. Numa, Nature **356**, 441 (1992).

[29] D. Boda, D. D. Busath, B. Eisenberg, D. Henderson, and W. Nonner, Phys. Chem. Chem. Phys., submitted.

[30] D. Boda, D. D. Busath, D. Henderson, and S. Sokołowski, J. Phys. Chem. B, **104**, 3875 (2000).

[31] D. Boda, D. Henderson, and D. D. Busath, J. Phys. Chem. B, **105**, 11574 (2001).

[32] D. Boda, D. Henderson, and D. D. Busath, Mol. Phys., in press (2002).

[33] W. H. Press, S. A. Teukolsky, W. T. Vetterling, B. P. Flannery, *Numerical Recipes in C: The Art of Scientific Computing,* 2nd ed. (Cambridge University Press, Cambridge, UK, 1992).

[34] W. Almers and E. W. McCleskey, J. Physiol., **353**, 585 (1984).

[35] P. Hess and R. W. Tsien, Nature, **309**, 453 (1984).

[36] P. G. Kostyuk, S. L. Mironov, and Y. M. Shuba, J. Membr. Biol., **76**, 83 (1983).

Figure captions

Figure 1. Example of a geometry used to model transport through an ion channel. The three-dimensional system is rotationally symmetric about the x-axis (dashed line). Axial cross-sections are shown at two different length scales. A lipid membrane (dark-grey area) contains a protein (black area) that provides a pore that connects the baths on the left and the right. The pore itself involves a short, narrow cylinder (the "selectivity filter") flanked by conical atria (b). For the discretized problem (Sec. 6), the three-dimensional geometry is represented by a stack of flat disks in the selectivity filter and spherical shells in the atria and baths whose axial interval is increased in proportion to the area of the shells. Panel (a) represents some shells in their actual geometric locations and spacing for the grid used in the simulations of Sec. 7; further shells extend to a radius of 1 μm. Panel (b) shows a subset of inner shells (the actual spacing is smaller). In total, the one-dimensional grid involves a stack of 110 disks and shells, with an increment of 0.02 nm between disks. This mapping of a three-dimensional geometry into one dimension would be exact for each of the cylindrical, spherical cone, or hemispherical regions alone, but becomes approximate when those regions are joined. The purpose of the nonuniform grid is to represent the selectivity filter in high spatial resolution while connecting this region to reservoirs of maintained concentrations and electrostatic potential a macroscopic distance away.

Figure 2. Test of the DFT for a two compartment equilibrium problem. In the left compartment ($x < 0$) was a 24 M fluid of half-charged oxygen ions. In the right compartment ($x > 0$) was 0.1 M of $CaCl_2$. The diameters are: Ca^{2+} 0.198 nm, Cl^- 0.362 nm, and $O^{-1/2}$ 0.28 nm. The concentrations after equilibration for $O^{-1/2}$, Ca^{2+}, and Cl^- are shown in panels (a), (b), and (c), respectively. In each panel is shown the reference concentration of the ion (dashed curve) used in the final iteration loop (Sec. 4.3). The + symbols represent the results of Monte Carlo simulations.

Figure 3. Tests of the DFT for a two compartment equilibrium problem. (a) The same simulation as in Fig. 2 except with 0.1 M NaCl in the right compartment with Na^+ given a diameter of 0.19 nm. (b) The same simulation as in Fig. 2 except with 22.8 M $O^{-1/2}$ in the left compartment and 0.1 M KCl in the right compartment with K^+ given a diameter of 0.266 nm.

Figure 4. For these simulations of a calcium-selective channel the structural particles are eight half-charged oxygen ions confined to the selectivity filter as described in the text. The diffusion coefficient profiles of the permeating particles (Ca^{2+}, Na^+, Cl^-, and H_2O) are piecewise constant profiles that are filtered using a 0.2 nm Gauss filter to produce a smooth profile. In the bath and pore, the piecewise constant diffusion coefficients are: Ca^{2+} 7.9×10^{-10} and 10^{-13} m^2/s, Na^+ 1.33×10^{-9} and 3.25×10^{-12} m^2/s, Cl^- 2.03×10^{-9} and 3.25×10^{-12} m^2/s, H_2O 2.13×10^{-9} and 2.13×10^{-11} m^2/s. The particle diameters are: Ca^{2+} 0.2 nm, Na^+ 0.2 nm, Cl^- 0.362 nm, $O^{-1/2}$ 0.28 nm, and H_2O 0.28 nm. The dielectric coefficient is 78.4 everywhere. In the experiment, there is 0.1 M NaCl in both baths and $CaCl_2$ is added to the right bath. The results at $[Ca^{2+}] = 10^{-7}$ M (dotted lines), 10^{-5} M (short-dashed lines), 10^{-3} M (long-dashed lines), and 10^{-1} M (solid lines) are shown for a -50 mV applied electrostatic potential. (a) the electrostatic potential. (b) water concentrations. (c) oxygen concentrations. (d) calcium concentrations. (e) sodium concentrations. (f) chloride concentrations. Only the concentrations of the permeating ions vary substantially as Ca^{2+} is added, which is also reflected in the changing electrostatic potential. The grey-shaded zone marks the cylindrical part of the channel (1 nm). The profiles 1 nm outside the grey zone were compressed, resulting in apparent discontinuities in some profiles.

Figure 5. The current/voltage relations for the ionic conditions used in Fig. 4. The logarithms of the Ca^{2+} concentration in the right bath are indicated near the curves.

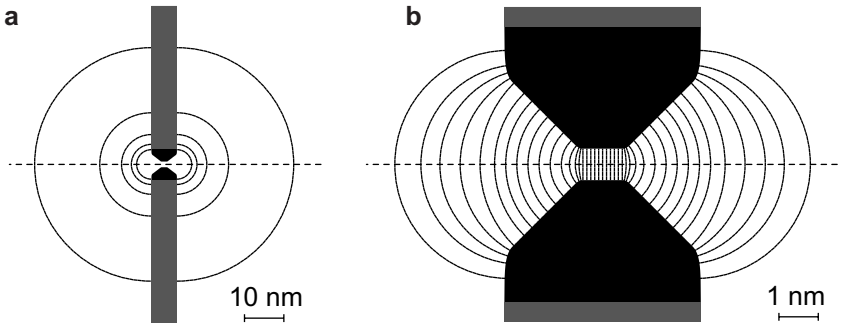

Figure 1 (Gillespie, Nonner & Eisenberg)

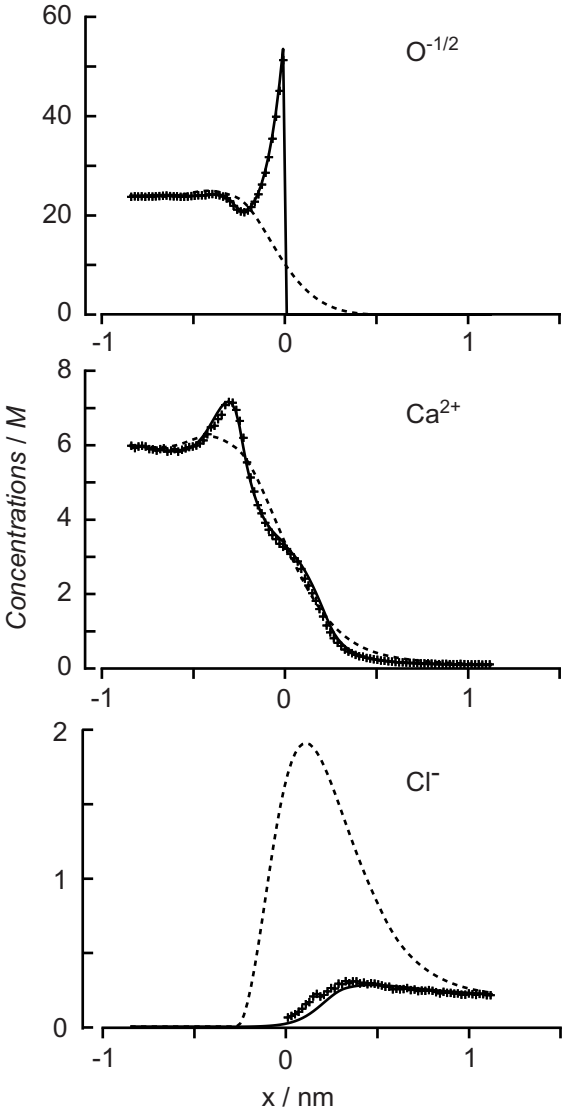

Figure 2 (Gillespie, Nonner & Eisenberg)

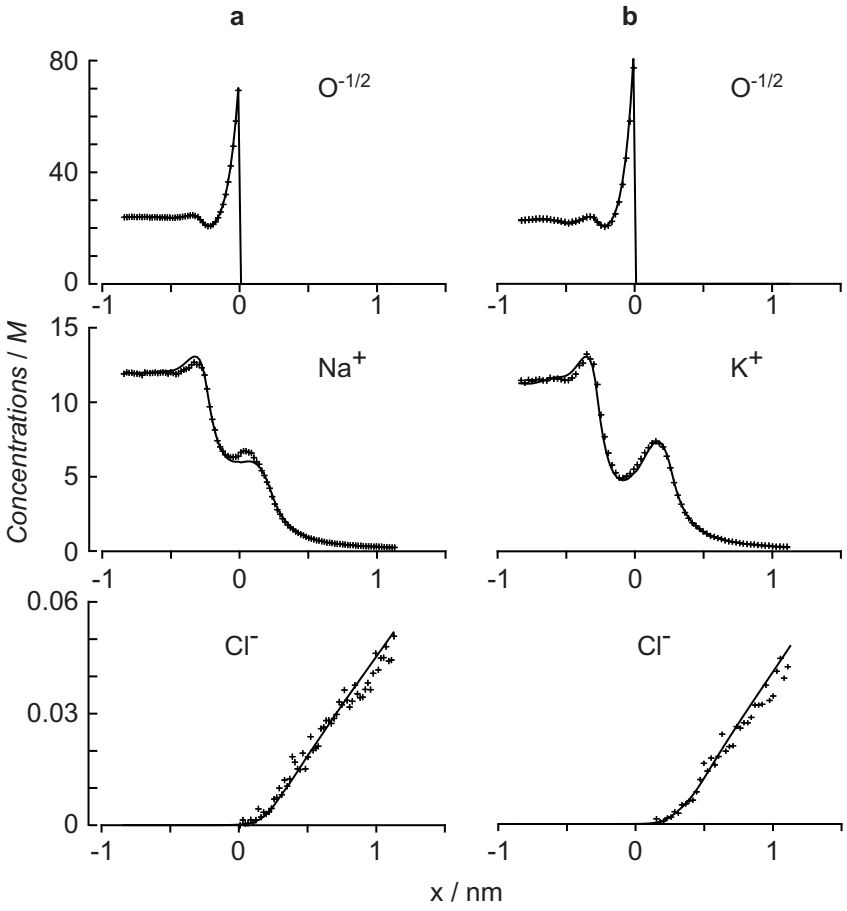

Figure 3 (Gillespie, Nonner & Eisenberg)

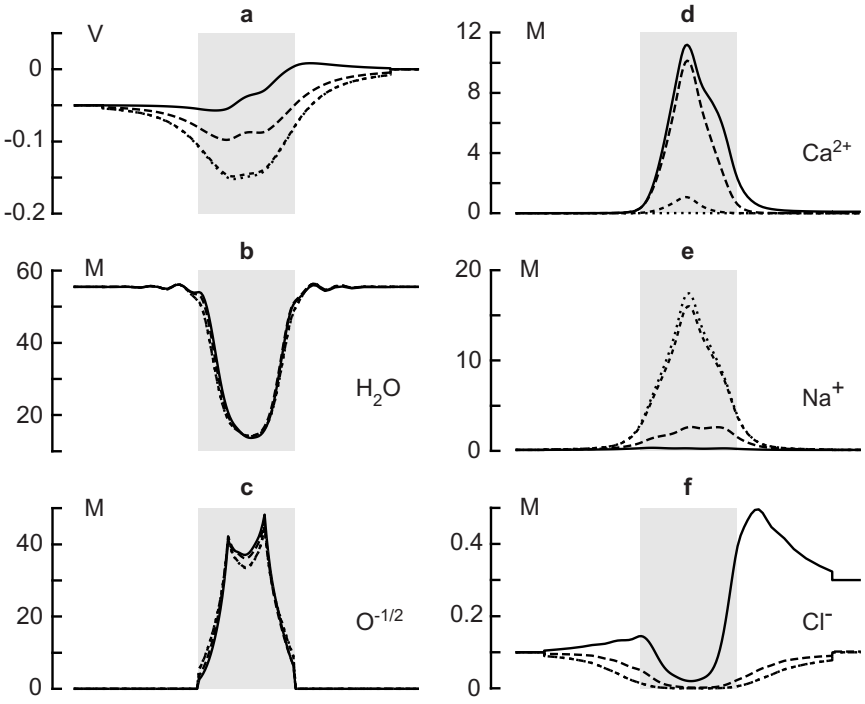

Figure 4 (Gillespie, Nonner & Eisenberg)

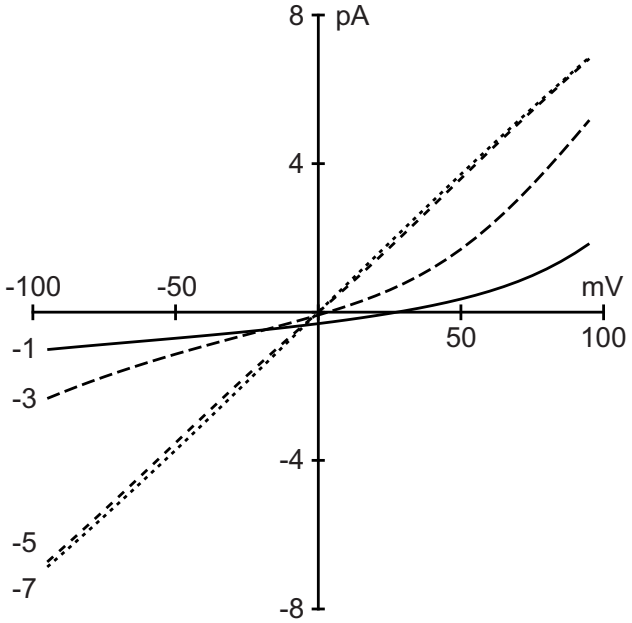

Figure 5 (Gillespie, Nonner & Eisenberg)